Supplementary Information (SI) for Chemical Science.

Supporting Information

A competition between 2D and 3D magnetic orderings in novel mixed valent copper frameworks

Yao Abusa, [a] Joshua Greenfield,[c] Gayatri Viswanathan,[ab] Smitakshi Goswami,[d] Emma Ross,[a] Philip Yox,[ab] Richeal Oppong,[ae] Iyanu Ojo,[a] Jifeng Liu,[f] Andrew Ozarowski,[g] Kirill Kovnir*[ab]

[a] *Department of Chemistry, Iowa State University, Ames, Iowa 50011, USA*

[b] *Ames National Laboratory, U.S. Department of Energy, Ames, Iowa 50011, USA*

[c] *Department of Chemistry, University of California, Davis, Davis, California 95616, USA*

[d] *Department of Physics and Astronomy, Dartmouth College, Hanover, NH 03755, USA*

[e] *Department of Materials Science and Engineering, Iowa State University, Ames, Iowa 50011, USA*

[f] *Thayer School of Engineering, Dartmouth College, Hanover, NH03755, USA*

[g] *National High Magnetic Field Laboratory, Florida State University, Tallahassee, Florida 32310, USA*

Corresponding author: Dr. Kirill Kovnir, kovnir@iastate.edu

Experimental Details

Scanning Electron Microscopy and Energy Dispersive X-ray Spectroscopy (SEM/EDS)

A FEI Quanta 250 field-emission SEM equipped with an EDS detector (Oxford X-Max 80, ThermoFischer Scientific, Inc.) was used to study selected ACu$_5$Br$_4$(COOH)$_4$ crystals. Large plate-like crystals were selected and mounted on double-sided adhesive carbon tape for the measurements. Samples were exposed to a 15 kV accelerating voltage and backscattered electron images were collected. Several crystals and sites were probed and averaged to quantify heavier elements (alkali metals, Cu, Br) and confirm the presence of N in (NH$_4$)Cu$_5$Br$_4$(COOH)$_4$. Acquired data were analyzed using the Aztec software. Compositions were normalized with respect to 4 Br atoms per formula unit.

Solid-State Diffuse Reflectance Spectroscopy

A Perkin Elmer Lambda 1050+ UV/Vis/NIR spectrophotometer with a 150 mm Spectralon-coated integrating sphere was used to collect diffuse reflectance data in the range of 250-2500 nm. Finely powdered samples were loaded into a spherical sample holder, pressed against a quartz lens, and held in place by a spring. The holder was placed at the reflectance port of the instrument while the specular port was open, with the beam adjusted and focused on the powder only. A Spectralon reference standard was used as a blank. Kubelka-Munk conversion of the diffuse reflectance data was used to determine the bandgaps by constructing Tauc plots and extrapolated the slopes to evaluate direct bandgaps, as well as other optoelectronic transitions.

Fourier Transform Infrared Spectroscopy (FT-IR)

FT-IR measurements were done on a Bruker IFS 66v/s FT-IR spectrometer under vacuum with 4 cm^{-1} resolution and 32 scans in the mid-IR region (400 to 4000 cm^{-1}). Samples were prepared by diluting with cesium iodide in a ratio of ~1:40 by weight. ACu$_5$Br$_4$(COOH)$_4$ samples were mixed with CsI powder, then finely ground and pressed into a thin pellet inside an N$_2$ glovebox. A blank (cesium iodide) was measured as a reference.

Thermogravimetric analysis/Differential scanning calorimetry (TGA-DSC)

Simultaneous thermogravimetric analysis (TGA) and differential scanning calorimetry (DSC) measurements were conducted using a Netzsch STA449 F1 TGA/DSC system. The samples were prepared by accurately measuring empty Al_2O_3 crucibles using the built-in balance, followed by measuring the combined mass of the samples and crucibles to obtain the exact sample mass. Temperature was increased at 10°C/min from approximately 30°C to 400°C under a 60 mL/min flow of ultra-high-purity argon. The samples were exposed to air between mass determination and the actual TGA-DSC measurement. Powder X-ray diffraction analyses of the samples after TGA-DSC experiments were performed.

Powder X-ray Diffraction and Rietveld refinement

Powder X-ray diffraction (PXRD) measurements were conducted on a benchtop Rigaku 600 Miniflex diffractometer employing Cu-K_α radiation (λ = 1.54059Å) with a Ni-K_β filter. Sample powders were sprinkled on zero-background silicon holders with a thin-layer of grease. High-resolution synchrotron PXRD datasets were collected at beamline 11-BM at the Advanced Photon Source at Argonne National Lab (APS ANL). Kapton capillaries were loaded with finely ground powders that were diluted with amorphous silica (SiO_2) to improve transmission. A wavelength of 0.412642 Å was employed.

General Structure Analysis System (GSAS-II) was used to perform Rietveld refinements of synchrotron PXRD data using the structural models obtained from SCXRD. The refinement was carried out in the 0.6-22° 2θ range for synchrotron data (λ = 0.412642 Å). The background and isotropic displacement parameters were refined for all samples. Unit cell parameters and atomic occupancies were also refined. Difference curves and R_{wp} residuals were used to evaluate the agreement between the calculated and experimental diffraction patterns.

Single Crystal X-ray Diffraction

Single crystal X-ray diffraction (SCXRD) experiments were performed on a Bruker D8 Venture diffractometer with a Photon100 CMOS detector employing Mo-$K\alpha$ radiation (λ = 0.71073 Å) at 100 K under a dry N_2 stream. Structure determination and crystal structure refinement was performed using the SHELX software package. At the final stage of refinement, the occupancies of the atomic sites were refined. Most of the sites show no deviations from 100% occupancy, within one e.s.d. However, Cu sites in the Cu-Br layer exhibited vacancies and the refinement of site occupancies resulted in substantial reduction of the *R*-values. CCDC files #2412816-2412819 contain the supplementary crystallographic data for this paper. These data can be obtained free of charge via www.ccdc.cam.ac.uk/data_request/cif, by emailing data_request@ccdc.cam.ac.uk, or by contacting The Cambridge Crystallographic Data Centre, 12 Union Road, Cambridge CB2 1EZ, UK; fax: +44 1223 336033.

Electron Paramagnetic Resonance (EPR) Spectroscopy

High-field, high-frequency EPR spectra at temperatures ranging from *ca.* 5 K to 290 K were recorded on a home-built spectrometer at the EMR facility of the National High Magnetic Field Laboratory (NHMFL). The instrument is equipped with a superconducting magnet (Oxford Instruments) capable of reaching a field of 17 T. Microwave frequencies over the range 52–630 GHz were generated by a phase-locked Virginia Diodes source, producing a base frequency of 8-18 GHz, which was multiplied by a cascade of frequency multipliers. The instrument is a transmission-type device and uses no resonance cavity. The EPR spectra and magnetic data were simulated using software written by Dr. Andrew Ozarowski (NHMFL), available from the author upon request.

Magnetic measurements

Magnetic properties were measured with a Quantum Design MPMS-XL SQUID magnetometer, with temperature-dependent magnetic susceptibility collected from 2-300 K in an applied field of either 0.01 T or 0.1 T and isothermal magnetization collected in an applied field of –7 T to +7 T at 2 K. Measurements were performed on polycrystalline samples and, in the case of $NH_4Cu_5Br_4(COOH)_4$ and $Rb_4Cu_5Br_4(COOH)_4$, on oriented single crystals.

Photoluminescence measurements

Photoluminescence (PL) measurements were conducted on single crystals of $A Cu_5Br_4(COOH)_4$ (A = NH_4, K, Rb) to probe their band-to-band transitions. The PL spectra were collected using Horiba Labram HR Evolution Raman spectrometer with a micro-PL setup employing a 50× objective lens and a 300 gr/mm grating at a temperature of 298 K. To ensure reproducibility and reduce the impact of site-specific variations, measurements were taken from multiple regions of each crystal. A 532 nm laser with a 100 mW output was used, attenuated by a 5% neutral-density filter. However, the optical efficiency of the equipment was determined to be 30%, rendering the effective power of the laser to be 1.5 mW.

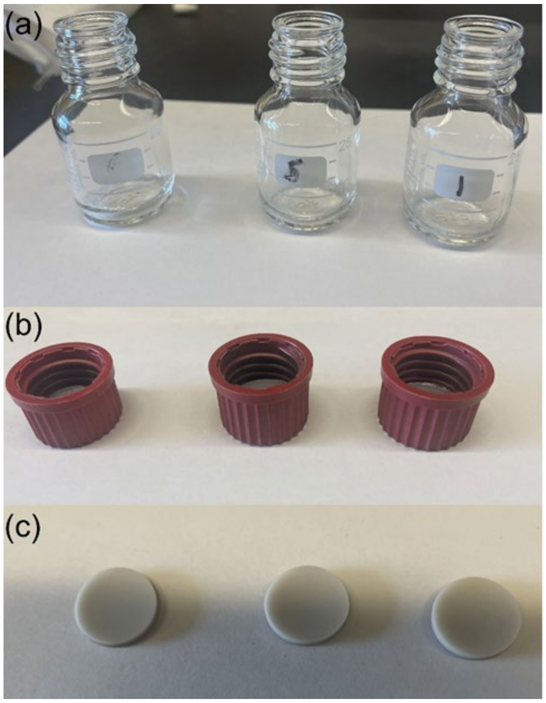

Figure S1. (a) Pyrex glass vessels, (b) plastic caps, and (c) Teflon cap liners employed in the synthesis of *A*$Cu_5Br_4(COOH)_4$ samples.

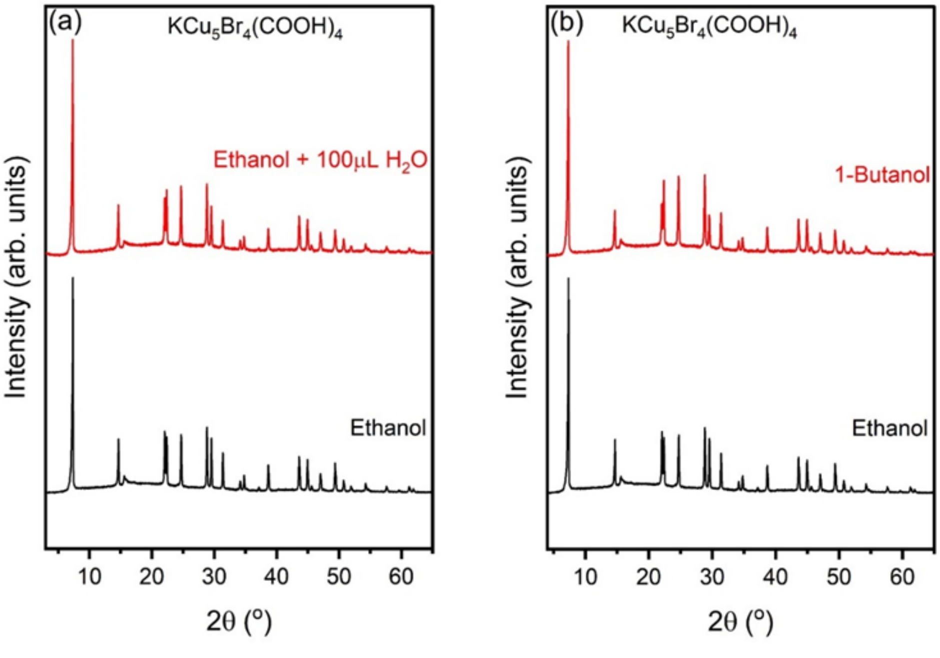

Figure S2. In-house powder X-ray diffraction patterns of $KCu_5Br_4(COOH)_4$ synthesized from $CuBr_2$, K_2CO_3, formic acid (HCOOH), and (a) ethanol + 100μL sacrificial water vs (b) 1-butanol, compared to pattern of $KCu_5Br_4(COOH)_4$ synthesized from ethanol only. Cu-K_α radiation (λ = 1.54059 Å).

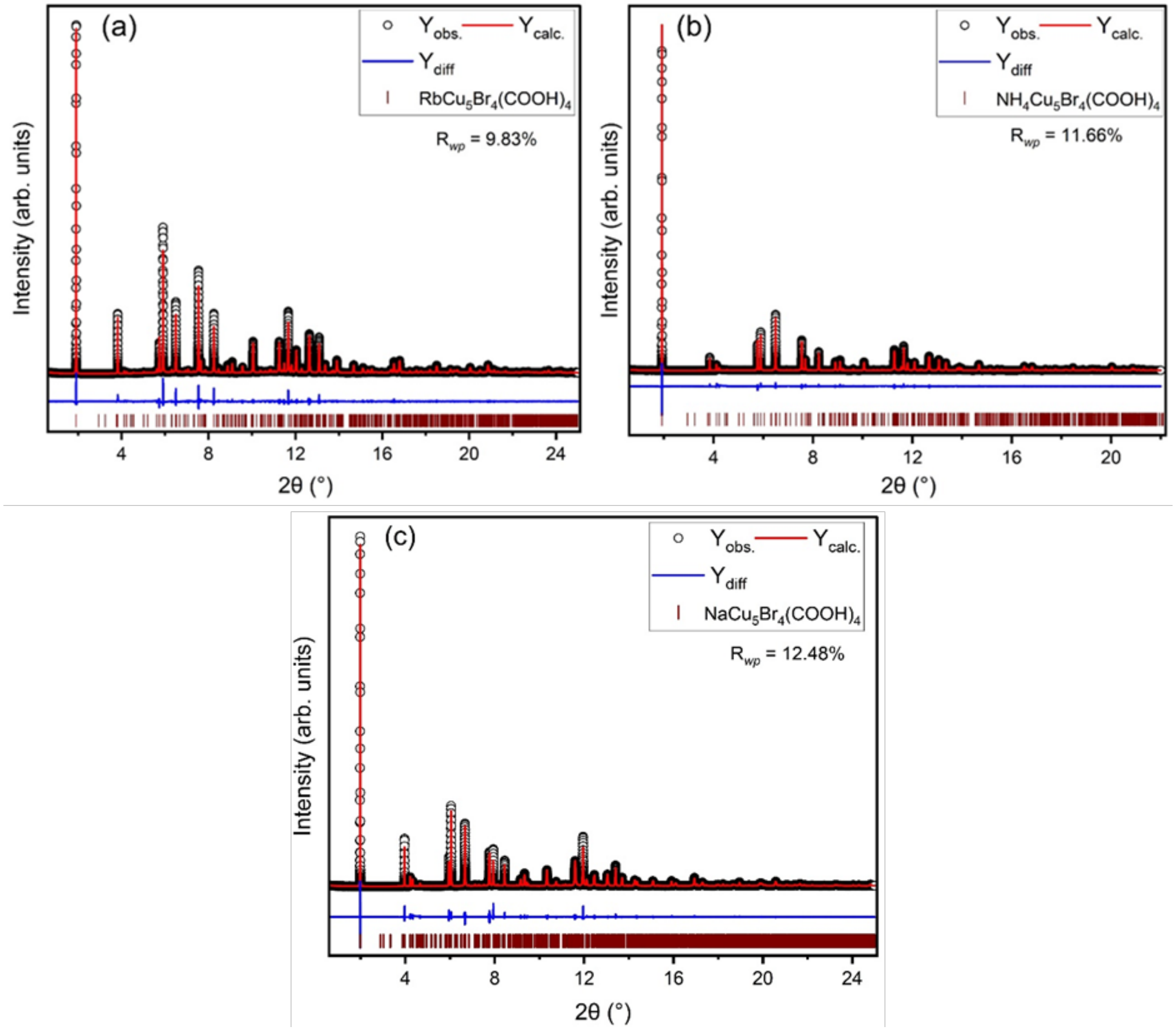

Figure S3. Rietveld refinement of room-temperature synchrotron PXRD patterns ($\lambda = 0.412642$ Å) for (a) $RbCu_5Br_4(COOH)_4$, (b) $(NH_4)Cu_5Br_4(COOH)_4$, and (c) $NaCu_5Br_4(COOH)_4$. Experimental data: black open circles. Calculated pattern: red line; difference profile: blue. Vertical maroon ticks indicate the peak positions for $ACu_5Br_4(COOH)_4$ (space group: $C2/m$ (No. 12) for Rb and NH_4; and $P2_1/c$ (No. 14) for Na).

Table S1. Ratio of C, H, O, and N in $ACu_5Br_4(COOH)_4$ obtained from CHN/O analysis.

$ACu_5Br_4(COOH)_4$	C	H	O	N
Na	4.05(2)	4.10(3)	7.8(5)	
K	4.09(2)	4.12(1)	7.6(5)	
NH_4	4.08(2)	8.10(8)	7.3(4)	0.93(2)
Rb	4.099(7)	4.09(4)	7.8(4)	

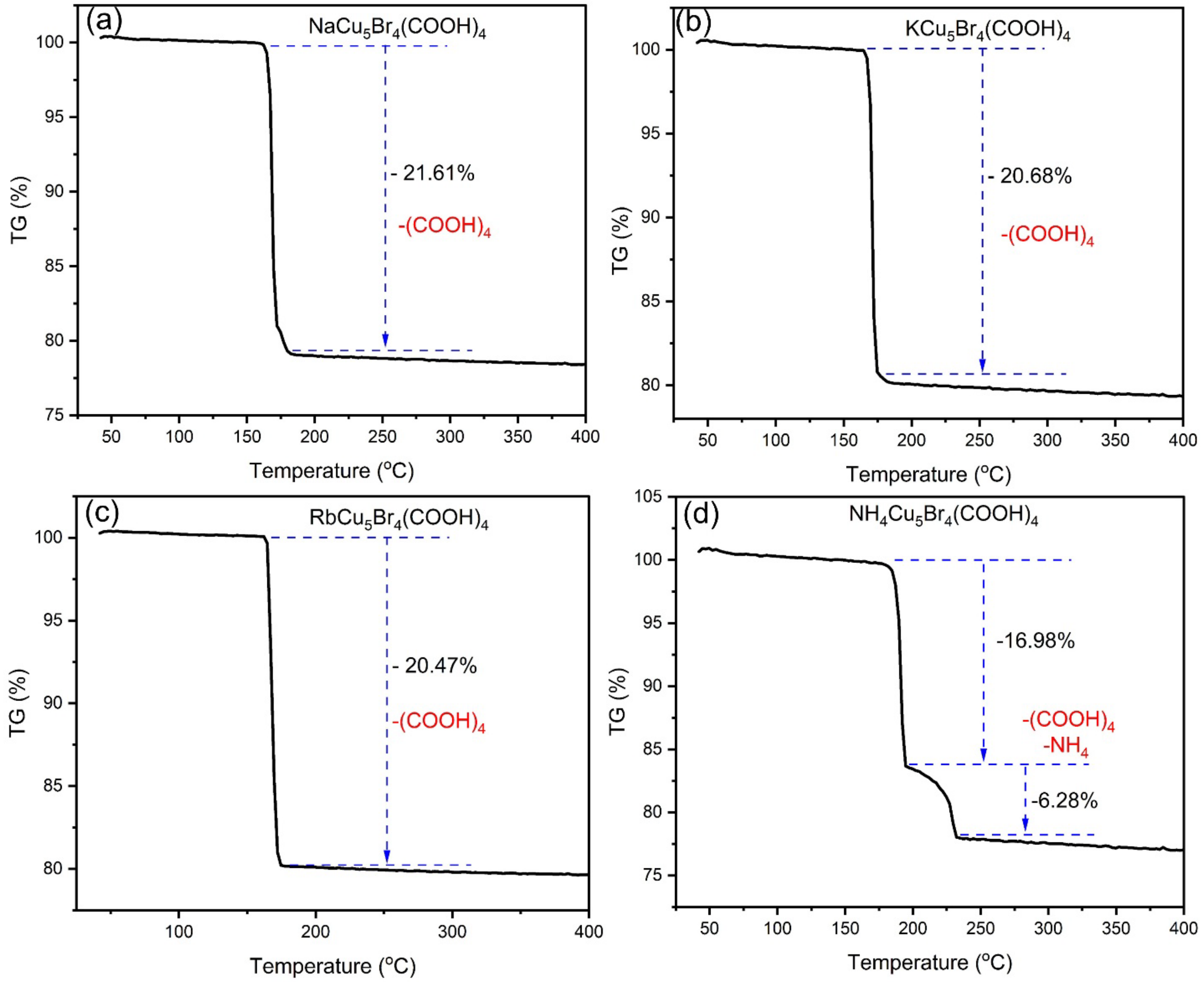

Figure S4. Thermogravimetric analysis (TGA) of ACu$_5$Br$_4$(COOH)$_4$ compounds (A^+ = Na$^+$, K$^+$, Rb$^+$, and NH$_4^+$) indicating percent weight losses corresponding to (COOH) and (NH$_4$) species.

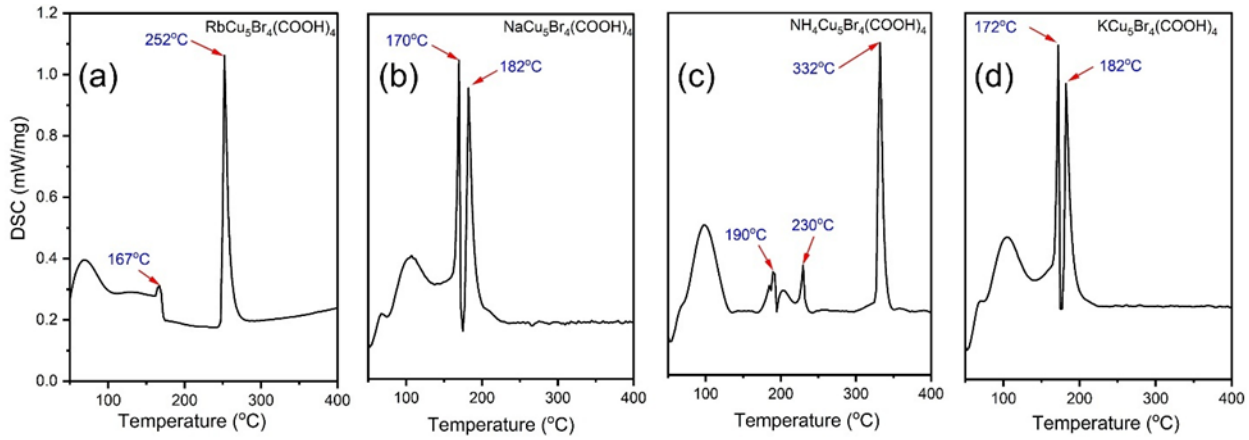

Figure S5. Differential scanning calorimetry (DSC) data of as-synthesized $A\mathrm{Cu_5Br_4(COOH)_4}$ compounds (A^+= $\mathrm{Na^+}$, $\mathrm{K^+}$, $\mathrm{NH_4^+}$, and $\mathrm{Rb^+}$) showing multiple thermal events upon heating up to 400°C. Thermal events above 200°C are attributed to the decomposition of the inorganic $\mathrm{ACu_5Br_4}$ framework, as confirmed by TGA and post-TGA PXRD, which indicate the prior loss of organic components.

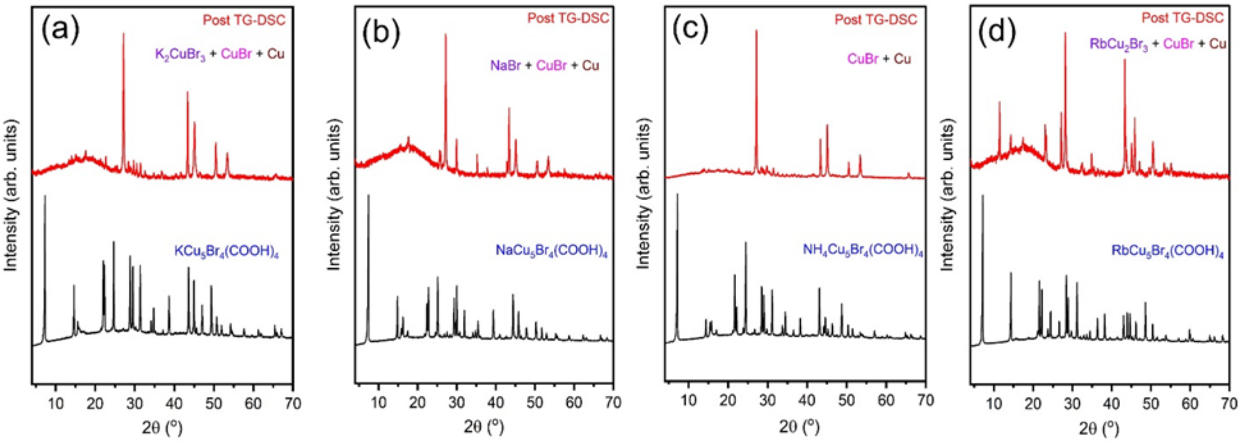

Figure S6. PXRD pattern of $A\mathrm{Cu_5Br_4(COOH)_4}$ samples (A = Na, K, $\mathrm{NH_4}$, and Rb) pre- (black pattern) and post-TGA (red pattern) collected with Cu-K_α radiation.

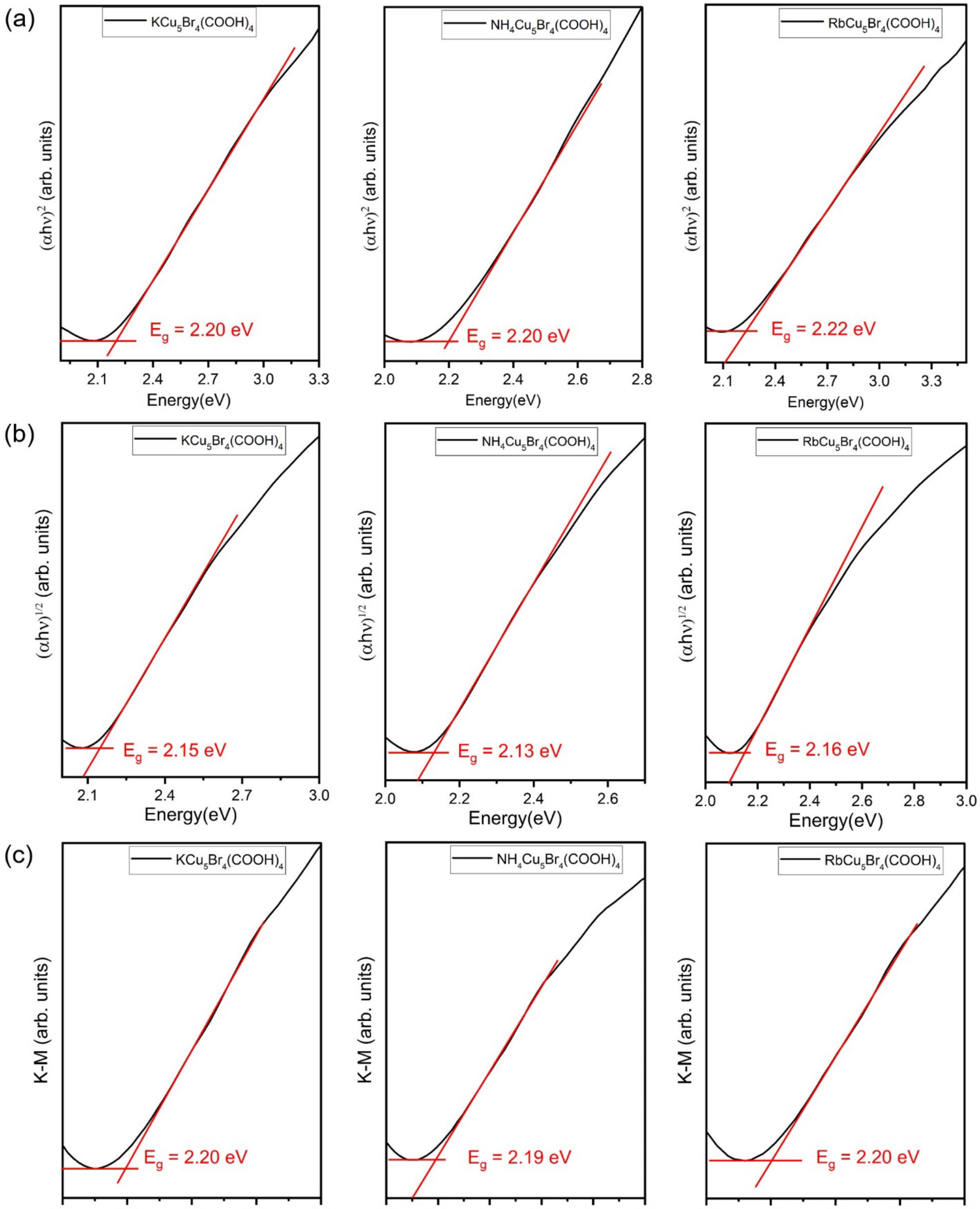

Figure S7. Tauc plots depicting (a) direct, (b) indirect transitions, and (c) Kubelka-Munk diffuse reflectance data for as-synthesized $ACu_5Br_4(COOH)_4$ (A = K, NH_4, and Rb) compounds.

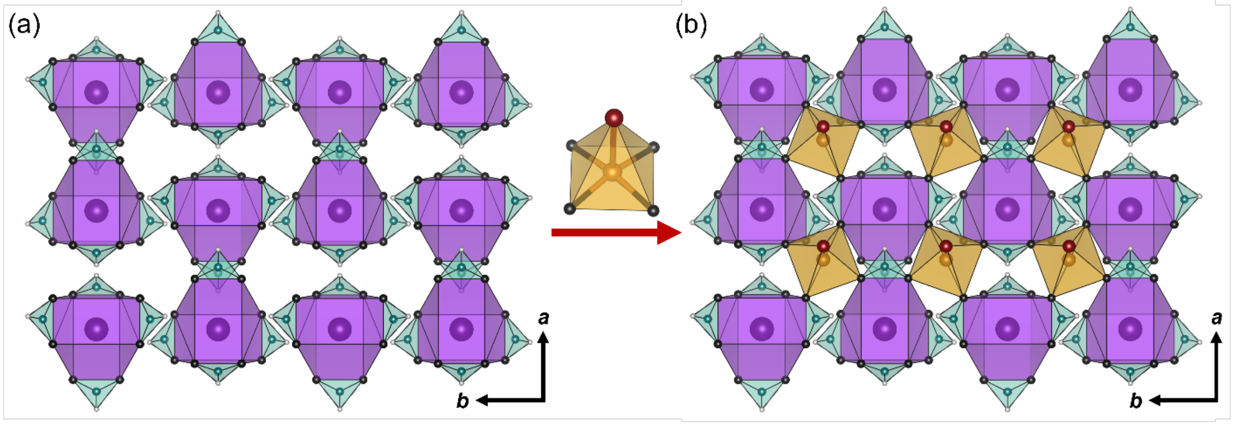

Figure S8. (a) A layer of isolated 0D [*A*(COOH)$_4$]$^{3-}$ rectangular antiprisms. (b) The O atoms of the formate ions form the base of [Cu(II)BrO$_4$] pseudo-square pyramidal units, helping to build the 3D architecture of the structure.

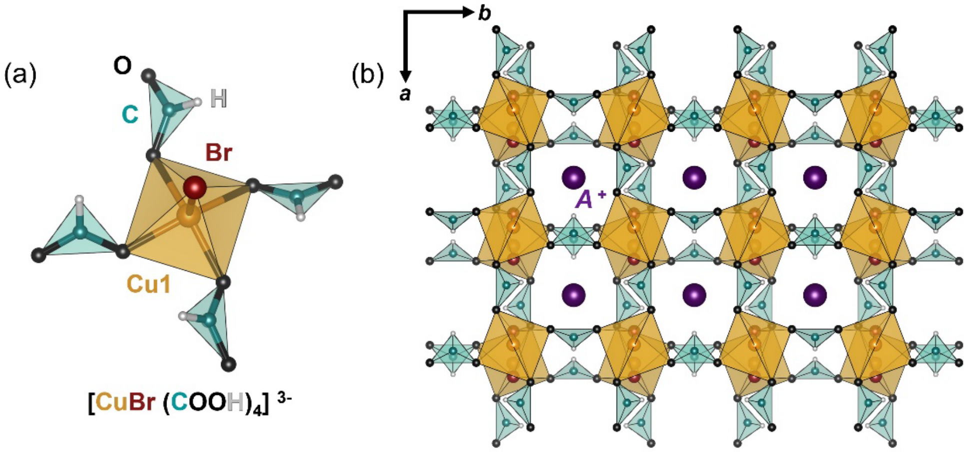

Figure S9. (a) Anti-anti planar coordination of Cu(II) ions by oxygen atoms from four different formate anions and one apical Br^{1-} ion, resulting in an overall pseudo-square pyramidal geometry. (b) The non-coplanar stacking of two Cu(II)-Br-formate layers in the unit cell.

Table S2. Single Crystal Data Collection and Structural Refinement Parameters for $A\mathrm{Cu_5Br_4(COOH)_4}$.

A	Na	K	NH$_4$	Rb
Space group	$P2_1/c$ (No.14)	$C2/m$ (No.12)		
Crystal system	Monoclinic			
Temp.(K)	100(2)			
a (Å)	12.1357(7)	11.3847(7)	11.4744(9)	11.443 (1)
b (Å)	11.1746(5)	11.3964(8)	11.4780(9)	11.455 (1)
c (Å)	11.1684(6)	12.3227(9)	12.519(1)	12.605 (1)
β (deg)	103.214(2)	103.363(3)	103.243(1)	103.207(6)
V (Å^3)	1474.5(1)	1555.5(2)	1604.9(2)	1608.6(3)
λ (Å)	Mo-K_α, 0.71073			
Z	4			
ρ (g cm^{-3})	3.79	3.66	3.70	3.99
$\theta_{min}, \theta_{max}$ [°]	2.51, 36.37	3.69, 32.99	3.69, 32.99	3.69, 32.99
data/param	6954/210	1890/118	2593/129	3224/118
R_1	0.021	0.025	0.024	0.029
wR_2	0.064	0.067	0.065	0.069
$G.O.F$	1.04	1.08	1.05	1.16
Δp [e Å^{-3}]	1.45, –0.98	1.48, –0.79	0.73, –0.75	1.23, –1.34

Table S3. Selected interatomic distances (Å) and angles (°) in $A\mathrm{Cu_5Br_4(COOH)_4}$.

Bonds	**K**	**NH$_4$**	**Rb**
Copper environment			
Cu(1)-O	1.951 (3) Å	1.949 (3) Å	1.949 (3) Å
Cu(1)-Br(1)	2.7001(6) Å	2.6967(5) Å	2.7003(6) Å
Cu(2)-Br(1)	2.5087(8) Å	2.5108(8) Å	2.5078(8) Å
Cu(2)-Br(2)	2.4682(9) Å	2.469(1) Å	2.4713(9) Å
Cu(2)-Br(3)	2.4698(9) Å	2.473(1) Å	2.4731(7) Å
Cu(3)-Br(1)	2.5065(8) Å	2.5146(8) Å	2.5137(7) Å
Cu(3)-Br(3)	2.4687(7) Å	2.4711(7) Å	2.4688(7) Å
Cu(4)-Br(2)	2.4694(7) Å	2.4728(7) Å	2.4696(7) Å
Cu(4)-Br(1)	2.5056(8) Å	2.5129(8) Å	2.5130(7) Å
O-Cu(1)-O	88.7(1)°	88.6(1)°	88.7(1)°
Br(1)-Cu(2)-Br(3)	108.28(3)°	109.18(4)°	108.89(4)°
Br(1)-Cu(2)-Br(2)	108.13(3)°	108.98(4)°	109.75(4)°
Br(1)-Cu(3)-Br(3)	109.70(1)°	109.14(2)°	109.33(1)°
Br(1)-Cu(4)-Br(2)	109.98(1)°	109.47(1)°	109.63(1)°
Formate environment			
C-O	1.264(5) Å	1.256(4) Å	1.258(3) Å
C-H	0.930(4) Å	0.951(4) Å	0.930(4) Å
O-C-O	120.3(4)°	121.7(4)°	121.3(4)°
O-C-H	119.9(2)°	119.1(4)°	119.3(2)°
A-O	2.827(3) Å		2.956(3) Å
O-A-O	92.4(1)°		90.37(9)°

Table S4. Selected interatomic distances (Å) and angles (°) in $NaCu_5Br_4(COOH)_4$.

Bonds	Na
Copper environment	
Cu(1)-O	1.955 (3) Å
Cu(2)-O	1.956 (2) Å
Cu(1)-Br(2)	2.720(1) Å
Cu(2)-Br(4)	2.724(1) Å
Cu(3)-Br(1)	2.5034(9) Å
Cu(3)-Br(2)	2.482(1) Å
Cu(3)-Br(4)	2.527(1) Å
Cu(4)-Br(2)	2.527(1) Å
Cu(4)-Br(3)	2.4574(9) Å
Cu(4)-Br(4)	2.482(1) Å
Cu(5)-Br(1)	2.429(1) Å
Cu(5)-Br(2)	2.5326(9) Å
Cu(5)-Br(3)	2.427(1) Å
Cu(5)-Br(4)	2.5303(9) Å
Cu(5)-Br(4)	2.482(1) Å
Cu(6)-Br(1)	2.43(3) Å
Cu(6)-Br(2)	2.45(2) Å
Cu(6)-Br(3)	2.48 (3) Å
Cu(6)-Br(4)	2.47(2) Å
O-Cu(1)-O	88.76(9)°
O-Cu(2)-O	89.18(9)°
Br(1)-Cu(3)-Br(4)	109.86(4)°
Br(2)-Cu(4)-Br(3)	109.70(4)°
Br(1)-Cu(5)-Br(4)	112.23(5)°
Br(2)-Cu(6)-Br(3)	104.3(9)°
Formate environment	
C-O	1.265 (4) Å
C-H	0.930 (3) Å
O-C-O	120.9(3)°
O-C-H	119.6(3)°
Na-O	2.615(3) Å
O-Na-O	90.93(8)°

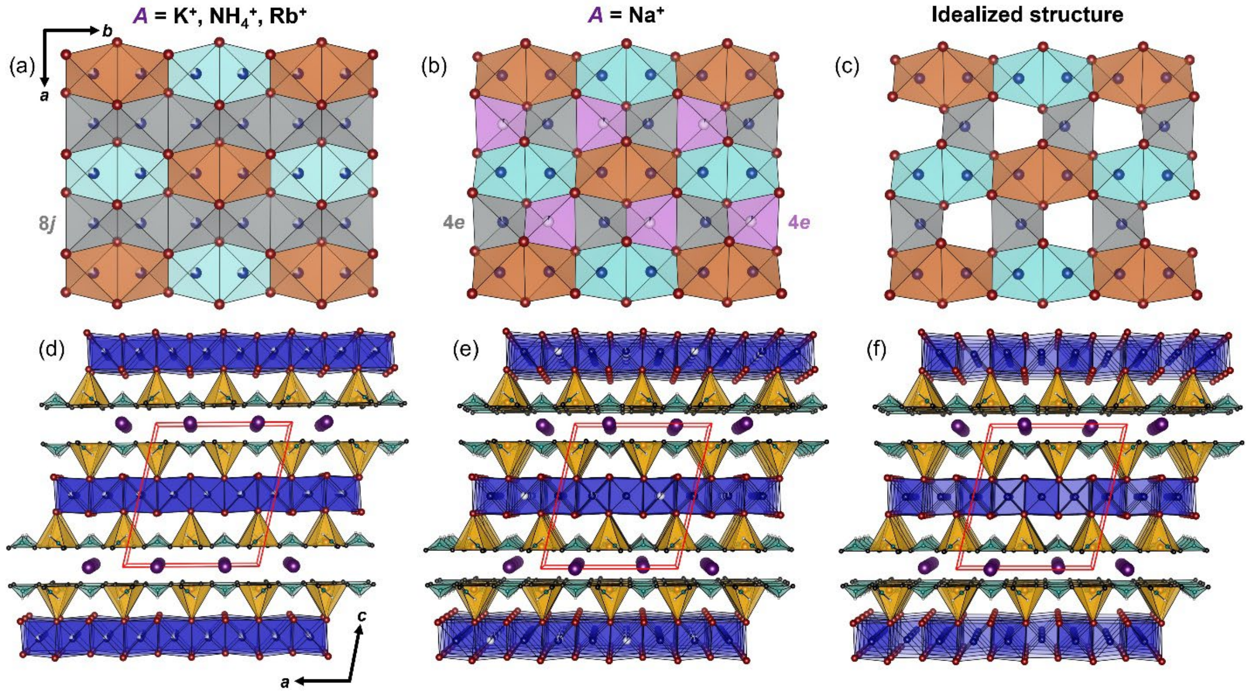

Figure S10. Comparison of vacancy-ordering of Cu^I atoms in Cu-Br layers between $ACu_5Br_4(COOH)_4$ ($A = K^+$, Rb^+, NH_4^+, and Na^+) structures and the idealized structure. (a) Larger cations result in a more disordered arrangement of Cu^I with three distinct crystallographic sites for Cu that are 75% occupied, while (b) smaller Na^+ promotes a more ordered structure with two fully ordered Cu sites and one almost fully occupied (gray) and one almost vacant Cu site (pink). These partially disordered sites in the Na-analog derive from splitting of the 8*j* site shown in (a) into two distinct 4*e* sites. (c) An idealized Cu-Br layer with three fully ordered Cu sites and one vacant 4*e* site. (d-f) Corresponding general views of the structures. *A*: purple, Cu(I): blue, Cu(II): yellow, C: cyan, O: black, H: grey, Br: red.

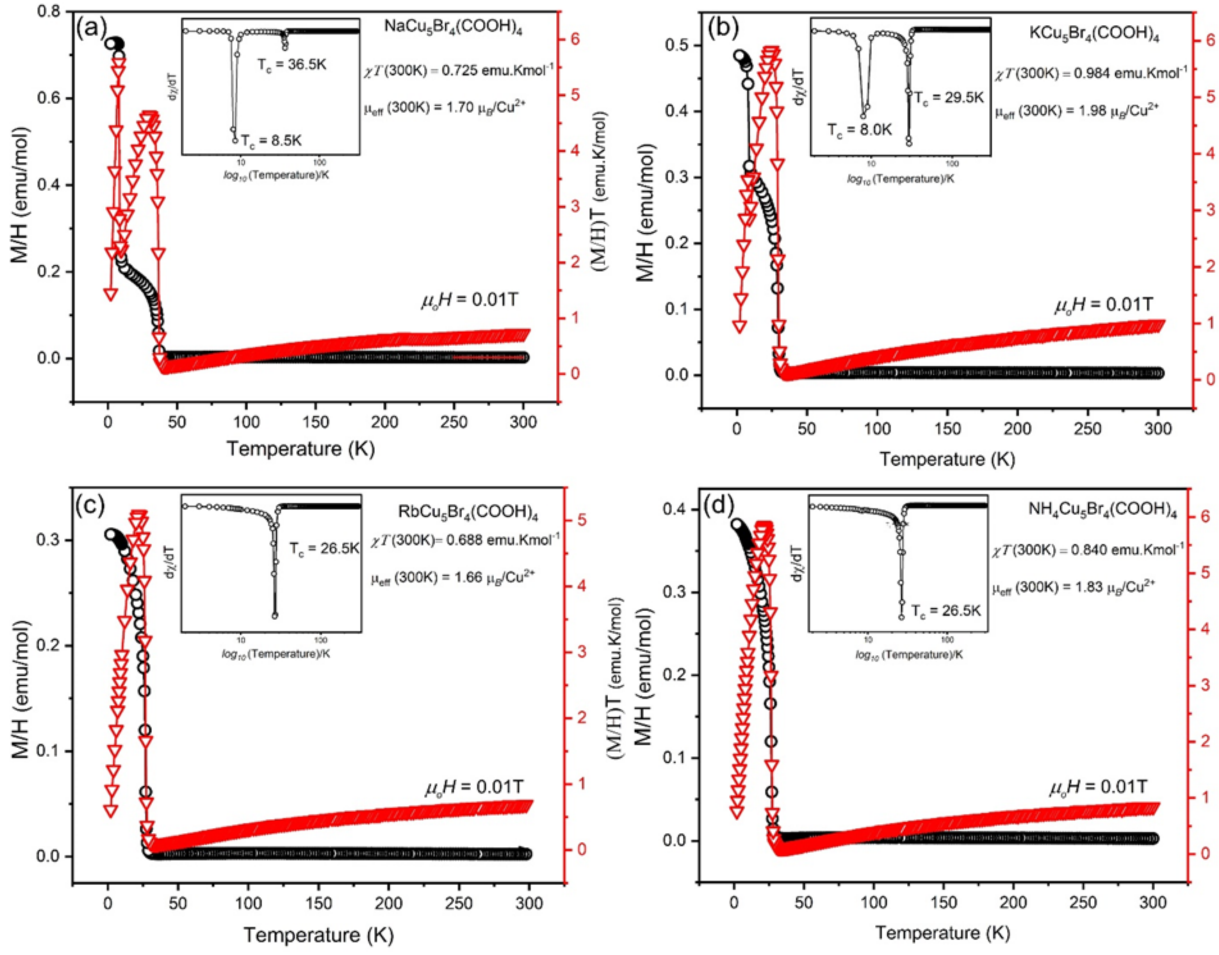

Figure S11. Temperature dependences of molar susceptibility (M/H, black) and χT product (red) of polycrystalline samples under an applied *dc* magnetic field of 0.01 T for (a) $NaCu_5Br_4(COOH)_4$, (b) $KCu_5Br_4(COOH)_4$, (c) $RbCu_5Br_4(COOH)_4$, and (d) $NH_4Cu_5Br_4(COOH)_4$. Insets: plots of the first derivative of molar susceptibility (dχ/dT) emphasizing magnetic transitions.

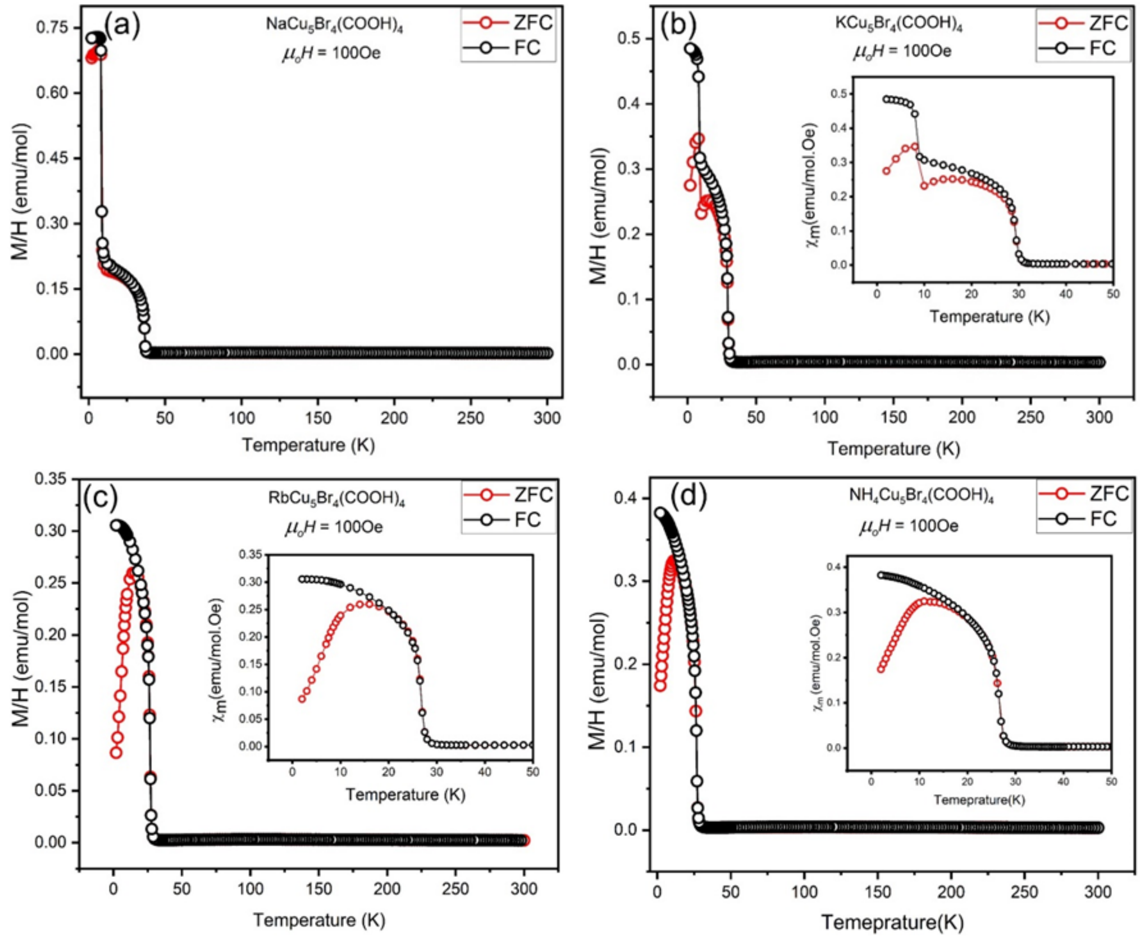

Figure S12. Field cooled (FC, black) and zero-field cooled (ZFC, red) plot of M/H against temperature under an applied *dc* magnetic field of 0.01 T from 2-300 K for polycrystalline samples of (a) $NaCu_5Br_4(COOH)_4$, (b) $KCu_5Br_4(COOH)_4$, (c) $RbCu_5Br_4(COOH)_4$, (d) $NH_4Cu_5Br_4(COOH)_4$. Insets: Low-temperature region of ZFC/FC data showing the onset of the bifurcation at various temperatures.

Table S5. 3D ordering temperature (T_C), strength of exchange interaction (J/k_B), intralayer Cu^{2+}–Cu^{2+} distances, and interlayer Cu^{2+}–Cu^{2+} bond distances: $\mathbf{D_1}$ (Cu^{2+}–Cu^{2+} distance bridged by Cu^{1+}–Br layers) and $\mathbf{D_2}$ (Cu^{2+}–Cu^{2} distance between formate layers separated by layers of A^+ cations) in crystal structures of $A$$Cu_5Br_4(COOH)_4$.

$A$$Cu_5Br_4(COOH)_4$	T_c (K)	J/k_B (K)	Cu^{2+} – Cu^{2+} distances		
A			Intralayer (Å)	$\boldsymbol{D_1}$ (Å)	$\boldsymbol{D_2}$ (Å)
Na	36.5	–101.5(4)	5.598	8.779	3.498
K	29.5	–107.9(8)	5.699	8.633	3.838
NH_4	26.5	–101.4(6)	5.737	8.592	4.087
Rb	26.5	–103.0(6)	5.728	8.602	4.155

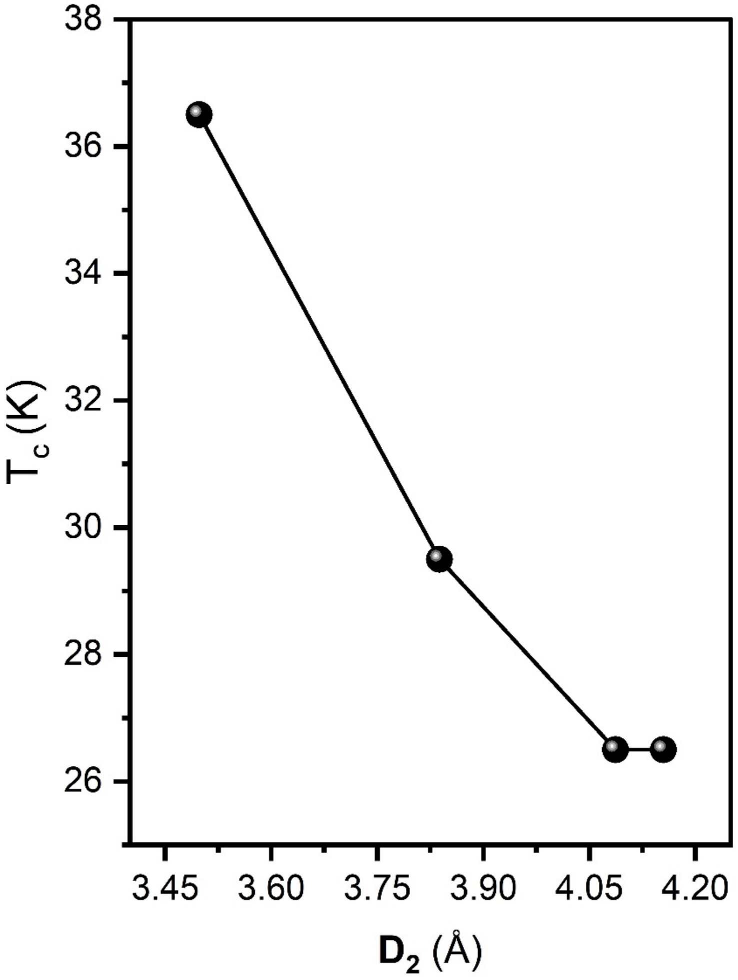

Figure S13. Plot of $\mathbf{D_2}$ (Cu^{2+}–Cu^{2+} distance between formate layers separated by layers of A^+ cations) against ferrimagnetic ordering temperature, T_c.

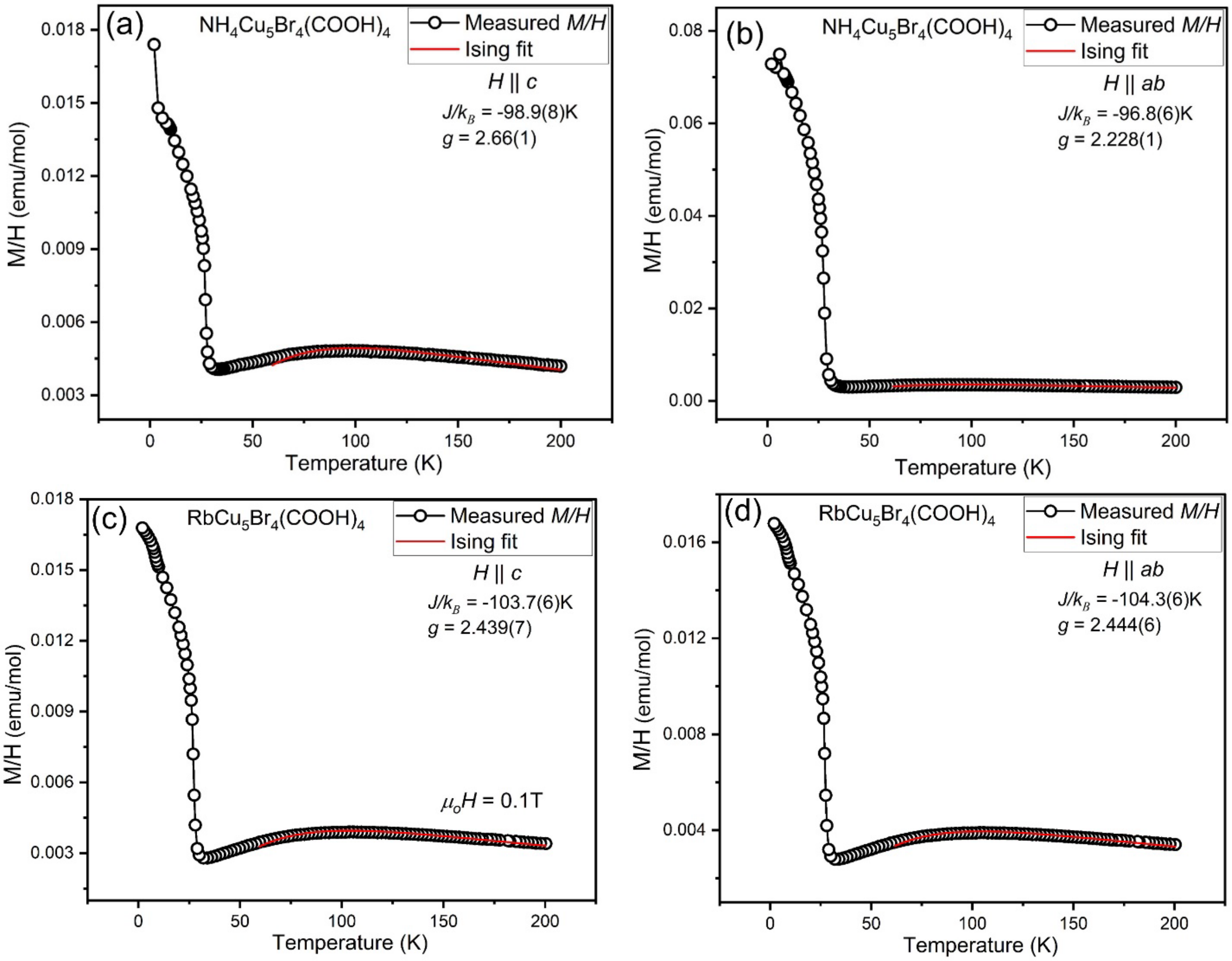

Figure S14. Plot of M/H versus T of oriented single crystals of (a , b) $NH_4Cu_5Br_4(COOH)_4$ and (c , d) $RbCu_5Br_4(COOH)_4$ under a field of 0.1 T. The red line shows the best fit using a simple Ising model for external magnetic field direction parallel to the direction of spin-quantization:

$$\chi_{\|} = \frac{N g_{\|}^{2} \mu_{B}^{2}}{2J} \left(\frac{J}{2kT}\right) e^{\left(\frac{J}{kT}\right)}$$

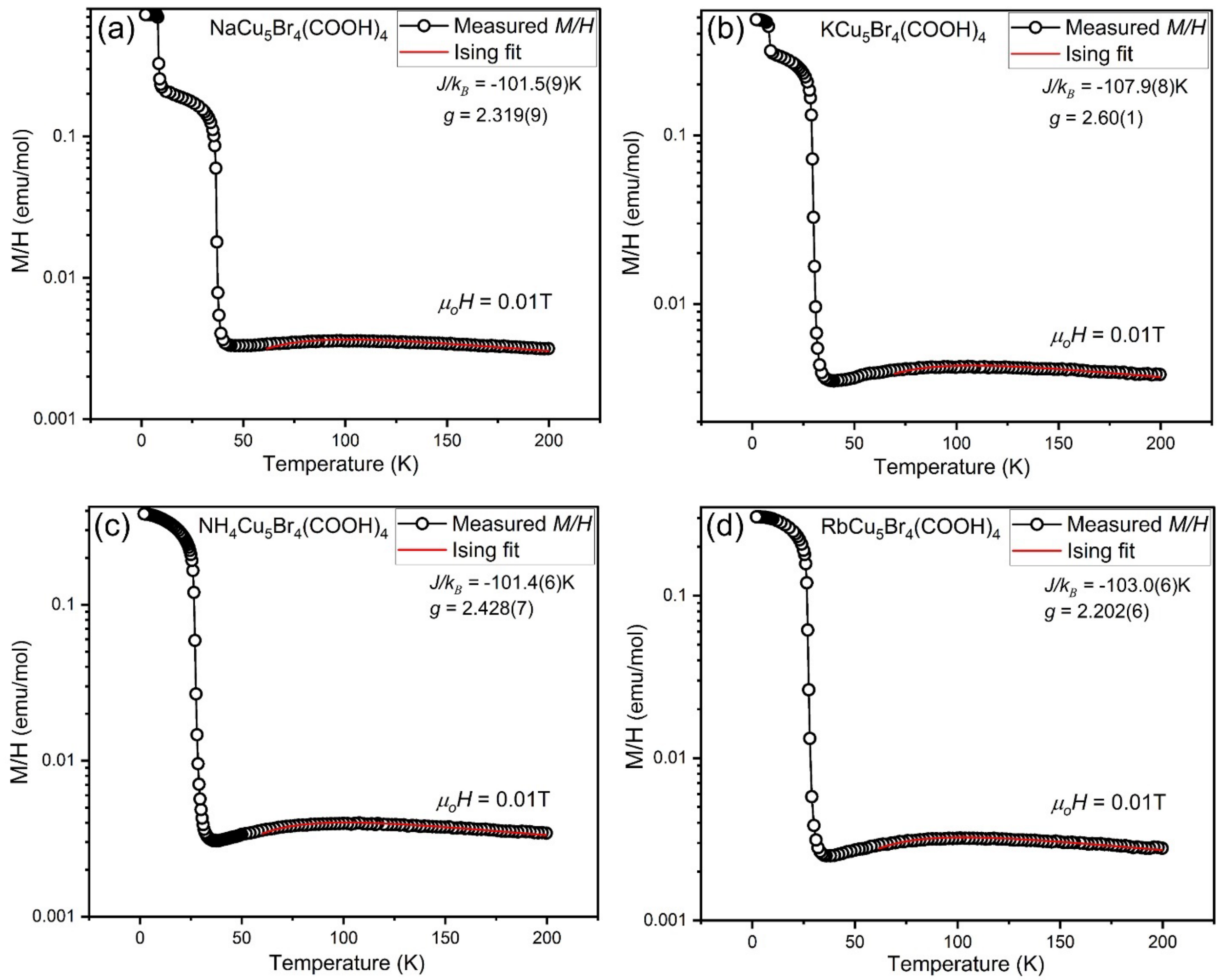

Figure S15. Plot of log of M/H versus T of polycrystalline samples for *A*$Cu_5Br_4(COOH)_4$ (*A* = Na, K, NH_4, Rb) under a 0.01T applied magnetic field. The red line shows the best fit using a simple Ising model.

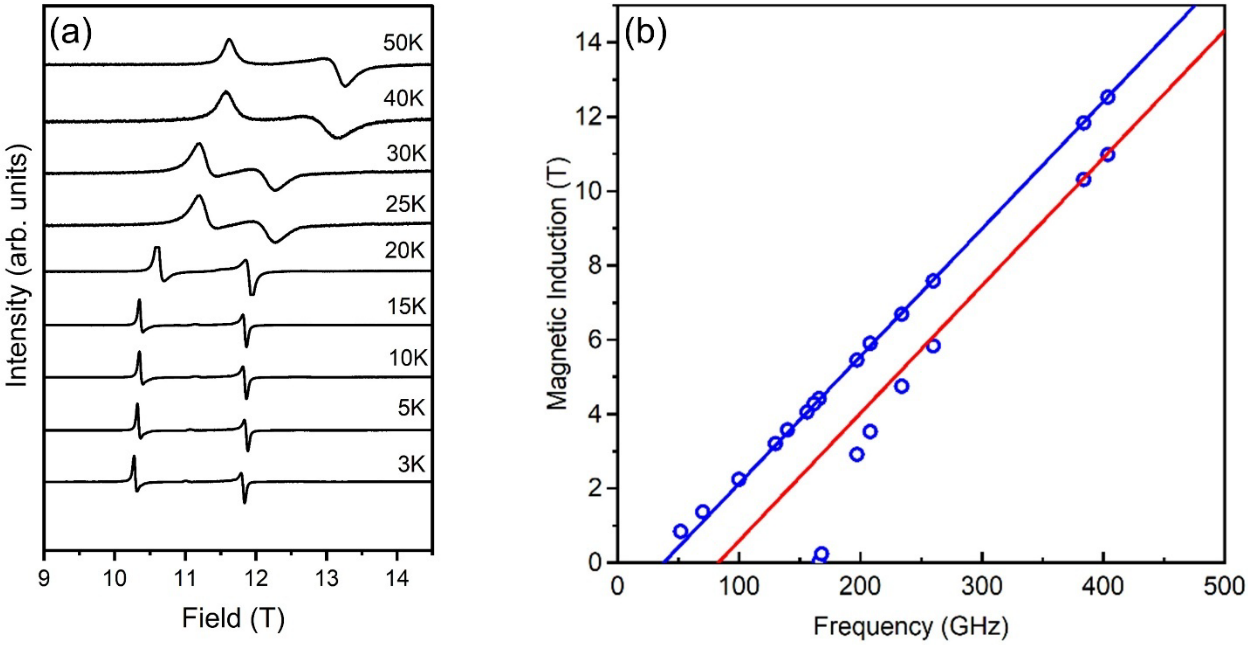

Figure S16. (a) Temperature-dependent EPR spectra of $NH_4Cu_5Br_4(COOH)_4$ measured at 384 GHz and (b) resonance field versus microwave frequency dependence in $NH_4Cu_5Br_4(COOH)_4$, read out from the spectra measured at various microwave frequencies over the range 25 to 495 GHz. Blue open circles represent resonances seen at 3 K. The straight blue line was calculated using $B = \mathrm{h}\cdot n/(\mu_B\cdot g)-B_{\mathrm{internal}}$, with $g = 2.085$ and $B_{\mathrm{internal}} = 1.30$ T. The second set of blue points do not exhibit a proper linear relationship approximated by the red line.

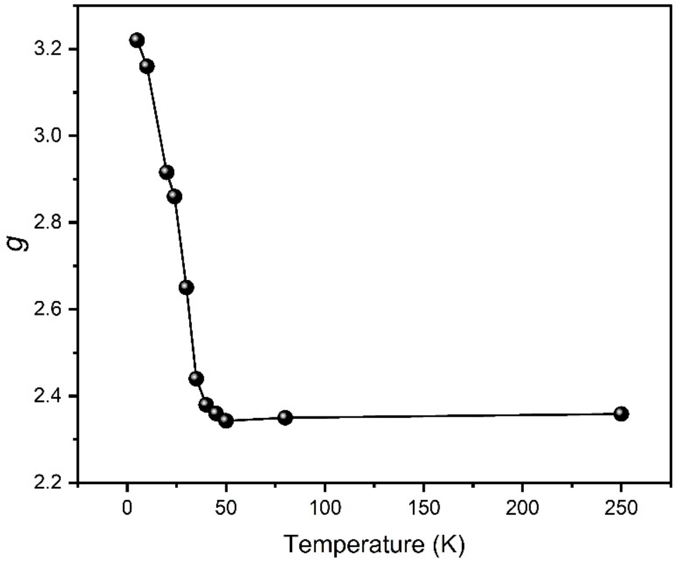

Figure S17. Temperature dependence of g-values calculated from $g_{eff}=\mathrm{h}\cdot \nu/(\mu_B\cdot \mathrm{B})$ and EPR spectra of $KCu_5Br_4(COOH)_4$.

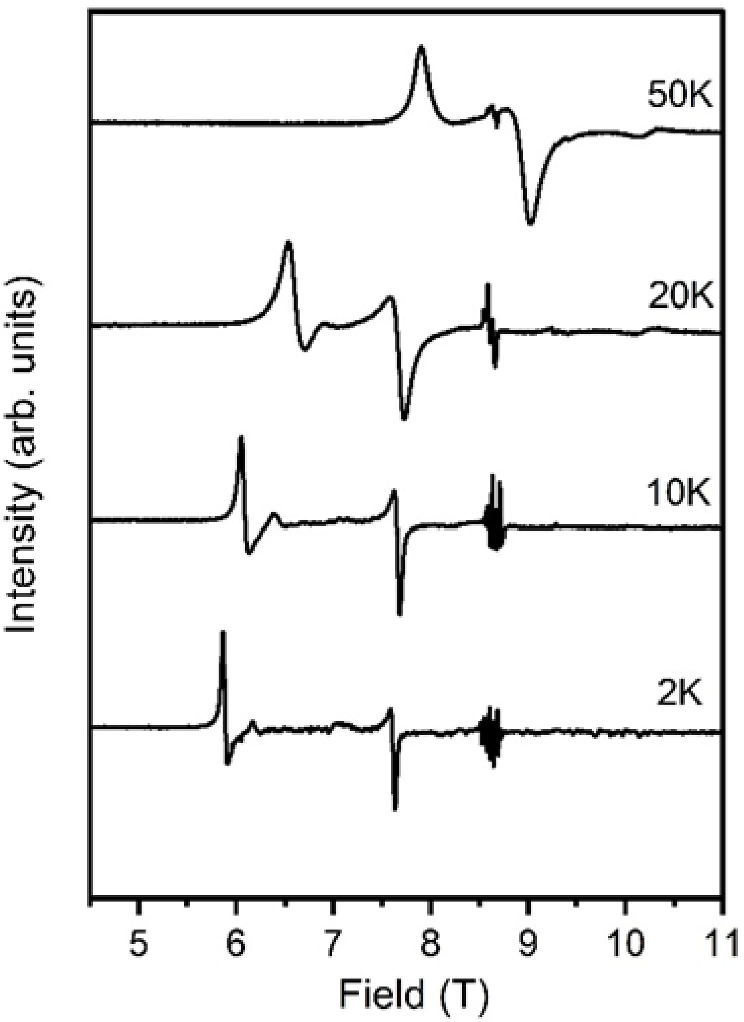

Figure S18. Temperature-dependent EPR spectra of $RbCu_5Br_4(COOH)_4$ measured at 260 GHz.

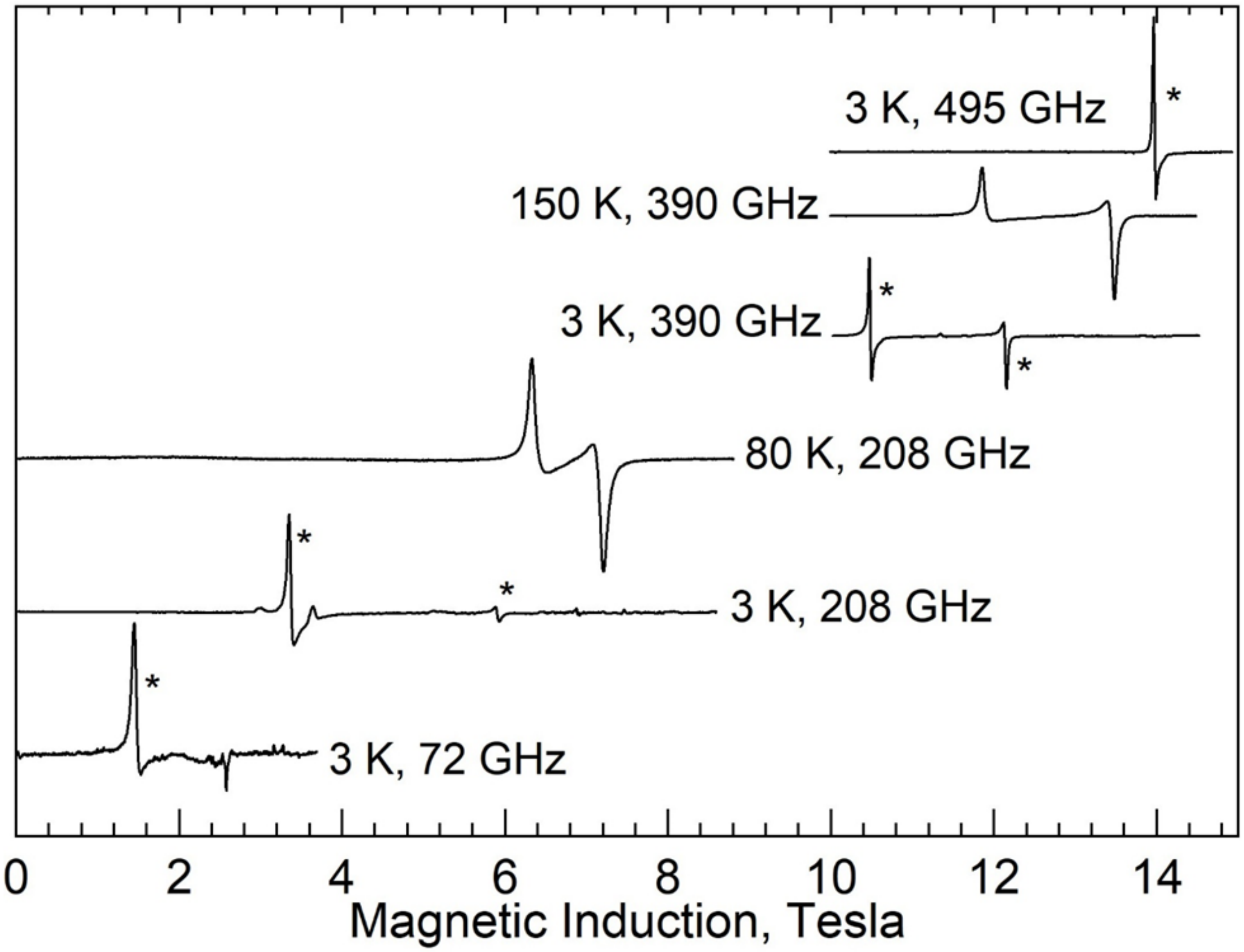

Figure S19. Frequency dependence of the high field EPR signals observed in $KCu_5Br_4(COOH)_4$ below and above the phase transition. The asterisks indicate the low-temperature features whose resonance fields are plotted in **Figure 6b** (main text). Note that only the low-field transition is seen at 495 GHz (the maximum field of our magnet is 14.9 T), and only the high-field feature is seen at 72 GHz. The low-field feature reaches the zero magnetic field at 168 GHz.

Table S6. Bond valence sum (BVS) estimates derived from single crystal diffraction data of *A*$Cu_5Br_4(COOH)_4$ using bond valence parameter of 2.03 for Cu^{1+}-Br^{1-} and 1.649 for Cu^{2+}-O^{2-}.

$KCu_5Br_4(COOH)_4$				
	Wyckoff sites	Site Occupancy	Bond Valence Sum (BVS)	Expected bond distance
Cu1	8*j*	1.00	1.820	1.988 Å (Cu1-O)
Cu2	4*h*	0.75	0.872	2.543 Å (Cu2-Br)
Cu3	8*j*	0.75	0.872	2.543 Å (Cu3-Br)
Cu4	4*h*	0.75	0.872	2.543 Å (Cu4-Br)
$RbCu_5Br_4(COOH)_4$				
	Wyckoff sites	Site Occupancy	Bond Valence Sum (BVS)	Expected bond distance
Cu1	8*j*	1.00	1.839	1.988 Å (Cu1-O)
Cu2	4*h*	0.75	0.863	2.543 Å (Cu2-Br)
Cu3	8*j*	0.75	0.864	2.543 Å (Cu3-Br)
Cu4	4*h*	0.75	0.863	2.543 Å (Cu4-Br)
$NH_4Cu_5Br_4(COOH)_4$				
	Wyckoff sites	Site Occupancy	Bond Valence Sum (BVS)	Expected bond distance
Cu1	8*j*	1.00	1.847	1.988 Å (Cu1-O)
Cu2	4*h*	0.75	0.860	2.543 Å (Cu2-Br)
Cu3	8*j*	0.75	0.860	2.543 Å (Cu3-Br)
Cu4	4*h*	0.75	0.859	2.543 Å (Cu4-Br)
$NaCu_5Br_4(COOH)_4$				
	Wyckoff sites	Site Occupancy	Bond Valence Sum (BVS)	Expected bond distance
Cu1	4*e*	1.00	1.795	1.988 Å (Cu1-O)
Cu2	4*e*	1.00	1.794	1.988 Å (Cu2-O)
Cu3	4*e*	1.00	1.151	2.543 Å (Cu3-Br)
Cu4	4*e*	1.00	1.151	2.543 Å (Cu4-Br)
Cu5	4*e*	0.94	1.129	2.543 Å (Cu5-Br)
Cu6	4*e*	0.06	0.074	2.543 Å (Cu6-Br)